nature biotechnology

Brief Communication

https://doi.org/10.1038/s41587-022-01603-9

Solid-phase capture and profiling of open chromatin by spatial ATAC

Received: 7 June 2022

Accepted: 7 November 2022

Published online: 5 January 2023

Check for updates

Enric Llorens-Bobadilla[1,5] ✉, Margherita Zamboni[1,2,5], Maja Marklund[2,5], Nayanika Bhalla[2], Xinsong Chen[3], Johan Hartman[3,4], Jonas Frisén[1] & Patrik L. Ståhl[2] ✉

Current methods for epigenomic profiling are limited in their ability to obtain genome-wide information with spatial resolution. We introduce spatial ATAC, a method that integrates transposase-accessible chromatin profiling in tissue sections with barcoded solid-phase capture to perform spatially resolved epigenomics. We show that spatial ATAC enables the discovery of the regulatory programs underlying spatial gene expression during mouse organogenesis, lineage differentiation and in human pathology.

In multicellular organisms, cells progressively acquire specialized gene expression programs according to their position within a tissue[1]. Cell type-specific gene expression patterns result in part from the interaction between the transcriptional machinery and regulatory elements in the chromatin[2,3], a process dysregulated in disease[4,5]. Several methods have been developed to integrate gene expression and chromatin accessibility measurements in single cells[6–8]. Single-cell methods typically require tissue dissociation, and a wealth of spatial profiling methods has recently been developed to overcome this limitation, particularly at the transcriptome level[9]. However, we remain limited in our ability to interrogate chromatin accessibility with spatial resolution at a comparable scale because current spatial chromatin profiling approaches require custom microfluidics or microbiopsies[10,11].

We developed spatial ATAC to perform spatially resolved chromatin accessibility profiling in tissue sections. Spatial ATAC combines the assay for transposase-accessible chromatin and sequencing (ATAC-seq[12]) with tagmented DNA capture on a solid surface containing barcoded oligonucleotides, using an experimental platform analogous to our previous spatial transcriptomics approach[13]. First, we immobilize fresh frozen tissue sections onto barcoded slides and crosslink them to preserve chromatin structure during immunostaining. Immunostained sections are then imaged to register tissue coordinates and protein expression data. In the next step, Tn5 transposition is performed directly in permeabilized sections to tagment open chromatin. With the help of a chimeric splint oligonucleotide, DNA tagments are hybridized to spatially barcoded surface oligonucleotides during gentle tissue digestion. Ligation to the splint and subsequent polymerase gap fill and extension generate open chromatin fragments carrying a spatial barcode and PCR handles that are used for generating a sequencing library (Fig. 1a).

We performed spatial ATAC on replicate tissue sections from three stages of mouse gestational development (embryonic days E12.5, E13.5 and E15.5). Spatially barcoded open chromatin fragments showed high enrichment around transcriptional start sites (TSS), as well as nucleosome periodicity, hallmarks of ATAC-seq (Fig. 1b and Extended Data Fig. 1). We captured a median of 6,100, 3,100 and 7,100 unique fragments per 55 µm spot, with 14, 15 and 18% overlapping TSS in E12.5, E13.5 and E15.5 sections, respectively. These metrics are comparable with published single-nucleus and microfluidics-based spatial ATAC-seq data from the developing mouse (Extended Data Fig. 1a–c). Additionally, the aggregate distribution of fragments across the genome showed a very high concordance with reference single-nucleus ATAC-seq (snATAC-seq) datasets from the Encyclopedia of DNA Elements (ENCODE)[14] (Extended Data Fig. 1d,e). We next created a peak-spatial barcode count matrix using a common reference peak set across sections that were analyzed by latent semantic indexing (LSI) and uniform manifold approximation and projection (UMAP) for dimensionality reduction[15]. Unsupervised clustering identified 11 main clusters, which revealed high concordance with anatomical landmarks when projected onto their original spatial coordinates and were consistent, not only across replicate sections, but also across developmental stages and analytical strategies (Fig. 1c,d and Extended Data Figs. 2 and 3). This clustering further agreed with spatially aware non-negative matrix factorization dimensionality reduction and clustering[16], suggesting that

[1]Department of Cell and Molecular Biology, Karolinska Institute, Stockholm, Sweden. [2]SciLifeLab, Department of Gene Technology, KTH Royal Institute of Technology, Stockholm, Sweden. [3]Department of Oncology-Pathology, Karolinska Institute, Stockholm, Sweden. [4]Department of Clinical Pathology and Cancer Diagnostics, Karolinska University Hospital, Stockholm, Sweden. [5]These authors contributed equally: Enric Llorens-Bobadilla, Margherita Zamboni, Maja Marklund. ✉e-mail: enric.llorens@ki.se; patrik.stahl@scilifelab.se

https://doi.org/10.1038/s41587-022-01603-9

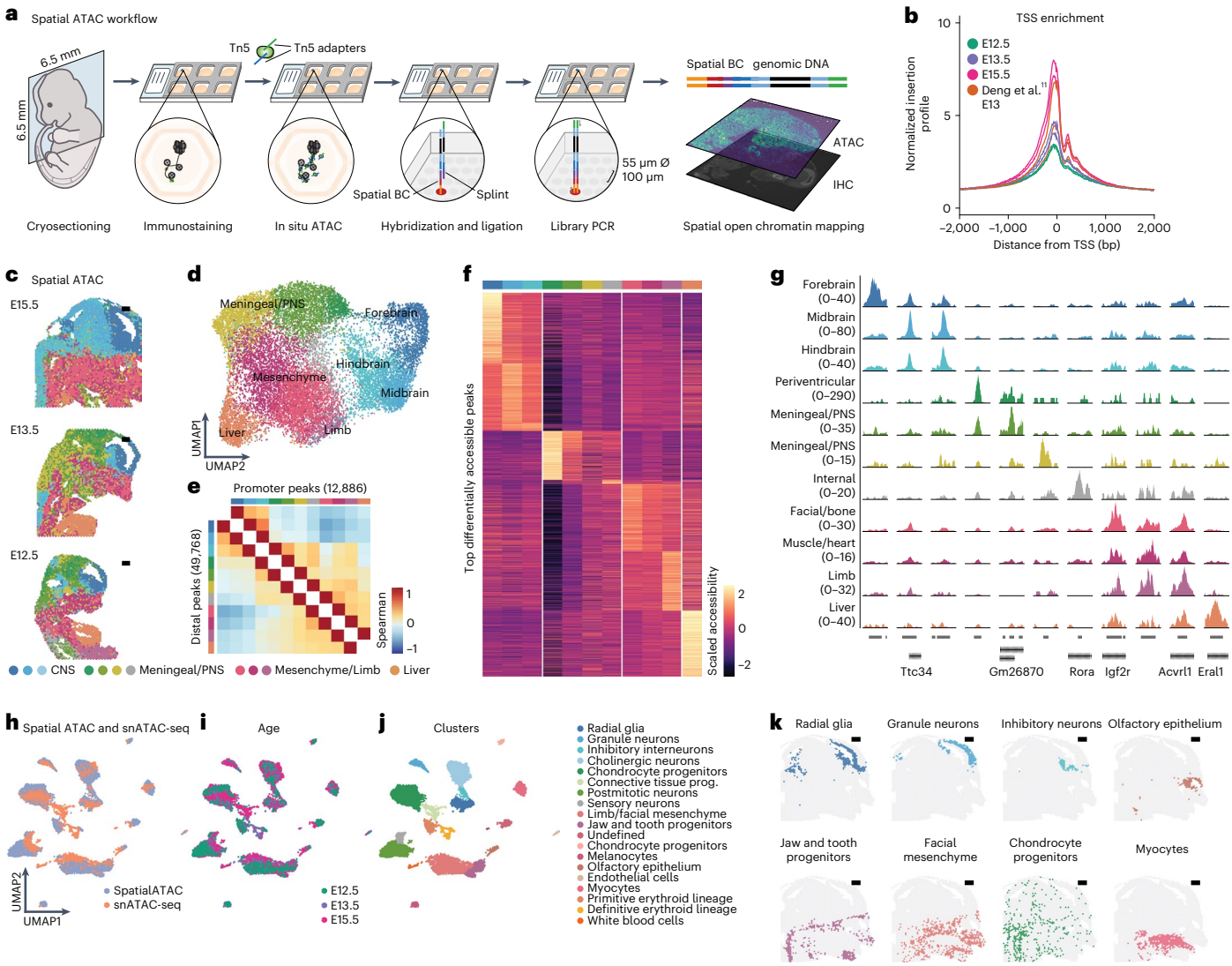

Fig. 1 | Workflow and spatial mapping of chromatin accessibility in mouse embryos. a, Schematic workflow of spatial ATAC. Transposition with Tn5 is performed on immunostained tissue cryosections immobilized on a barcoded slide (55 µm spot diameter; 100 µm interspot distance). Transposed fragments are surface-captured using a splint oligonucleotide, which is ligated and extended to allow the generation of a spatially barcoded DNA library. **b**, Enrichment of ATAC-seq fragments around the TSS in spatial ATAC performed on mouse embryos (E12.5, E13.5, E15.5) in comparison with spatial ATAC-seq E13 data from ref. 11. **c**, Clustering of spatial ATAC open chromatin fragments projected on their spatial location. **d**, UMAP of all spots from mouse embryo sections colored by cluster as in **c**. **e**, Cluster-wise correlation of the accessibility of the top 25% variable promoter (+1,000, −100 bp around the TSS) and distal peaks. **f**, Heatmap showing scaled accessibility of the top differentially accessible peaks per cluster. **g**, Genome tracks showing normalized spatial ATAC-seq fragment density for peaks showing cluster-specific accessibility. Cluster colors are consistent from **c**–**g**. **h**–**j**, UMAP showing the integration of spatial ATAC with snATAC-seq profiles from the same developmental stages colored by technology (**h**), developmental age (**i**) or clustering (**j**). **k**, Individual clusters from **j** projected onto their original spatial location in an E15.5 spatial ATAC section. Scale bars, 500 µm.

spatial location is a major source of variation in chromatin accessibility across and within developing tissues (Extended Data Fig. 4a–d). As expected, the dataset structure reflected variation in the accessibility of promoters and a larger set of distal peaks (Fig. 1e). Using differential accessibility analyses we found 18,000 differentially accessible peaks that showed specific patterns of accessibility across developing tissues (Fig. 1f, g).

We next computed gene activities (that is, accessibility at gene locus and promoter), which revealed 2,000 differentially accessible genes between clusters that were enriched for gene ontology terms characteristic of the respective tissue region (Extended Data Fig. 4e, f). For example, central nervous system clusters showed increased accessibility in genes known to be involved in neurogenesis (for example, *Sox1*, *Foxg1*, *Notch1*). Bone and muscle mesenchyme clusters showed increased accessibility in myofiber, collagen and TGF-b signaling genes (for example, *Myh9*, *Col1a1*, *Smad3*), while the fetal liver cluster was characterized by accessibility of genes involved in erythropoiesis (for example, *Hba-a1*, *Tal1*, *Sptb*). We next generated snATAC-seq profiles from matched developing embryos for direct comparison. Spatial ATAC spots integrated well with snATAC-seq data, which further increased clustering granularity within tissue structures (Fig. 1h–k). Genome-wide chromatin accessibility correlation across cell types was high between technologies, which allowed us to accurately predict the spatial location of individual cells (Extended Data Fig. 5).

Next, we sought to integrate spatial ATAC with Visium spatial transcriptomics. We performed Visium on tissue sections from the same developmental stages, which showed regionally consistent clustering and genes found as differentially accessible using spatial ATAC showed

https://doi.org/10.1038/s41587-022-01603-9

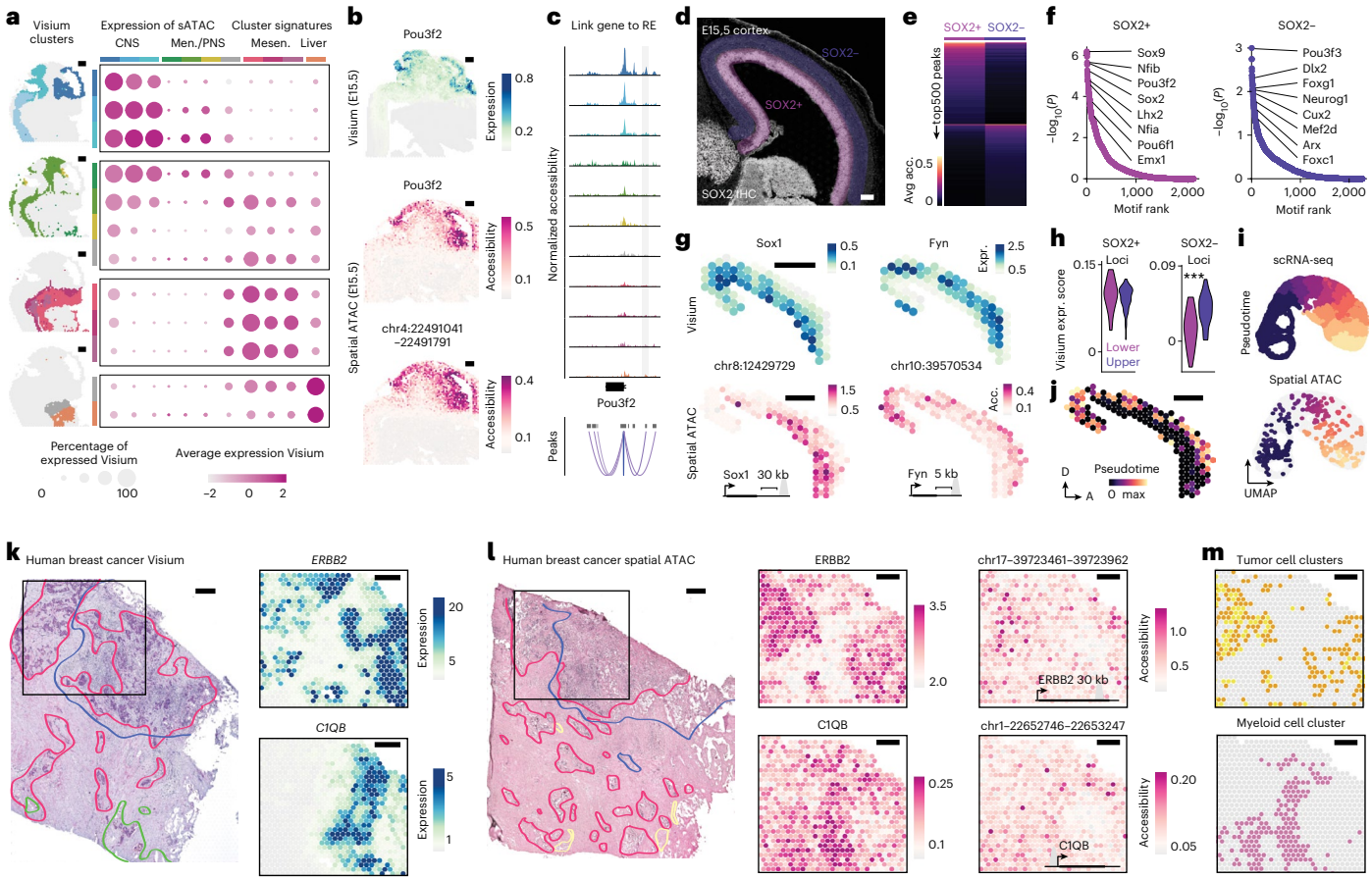

Fig. 2 | Spatial ATAC uncovers spatiotemporal patterns of regulatory element accessibility underlying gene expression. a, Visium gene expression signature scores for differentially accessible genes in spatial ATAC (sATAC) clusters. Visium clusters (left) on an E12.5 section for reference. CNS, central nervous system; Men./PNS, meninges/peripheral nervous system; and Mesen., mesenchyme. **b**, *Pou3f2* expression (top, cyan), gene activity and accessibility of a co-accessible distal regulatory element (magenta). **c**, Genomic track and co-accessibility scores for peaks around the *Pou3f2* locus. The distal element shown in **b** is highlighted in gray and tracks are colored according to spatial ATAC clusters. **d**, Inset of a SOX2-immunostained E15.5 spatial ATAC section ($n = 2$) with highlighted SOX2+ (progenitor, pink) and SOX2− (neuronal, purple) regions. **e**, Top 500 differentially accessible peaks by fold change in SOX2+ and SOX2− regions. Avg. acc., average accessibility. **f**, Motif enrichment analysis of peaks from **e**. Selected motifs for transcription factors expressed in the region are highlighted. *P* values by a one-sided hypergeometric test. **g**, Accessibility (Acc.) (spatial ATAC; magenta) and expression (expr.) of the nearest gene (Visium; cyan) for loci enriched in progenitor (*Sox1*) or neuronal (*Fyn*) regions. **h**, Gene signature score in lower and upper cortical regions for differentially accessible genes in SOX2+ and SOX2− regions. **i**, UMAP of integrated single-cell RNA-seq and spatial ATAC from the E15.5 developing cortex colored by pseudotime and split by technology. *P* values by Wilcoxon test (***<0.001). **j**, Pseudotime scores projected onto their spatial locations in a spatial ATAC E15.5 section. **k**, Hematoxylin and eosin image of a breast cancer section processed using Visium ($n = 1$) with overlaid pathologist annotations. Expression of *ERBB2* (HER2) and myeloid cell marker *C1QB* in the boxed inset. **l**, Annotated hematoxylin and eosin image of an adjacent (200 µm) section processed using spatial ATAC ($n = 3$). On the right, accessibility of the *ERBB2* locus, *C1QB* locus and two associated regulatory regions in the boxed inset (right). **m**, Spatial interaction between tumor cell and myeloid cell clusters at the tumor interface. Pathology is denoted as follows: red, invasive cancer; blue, tumor infiltrating lymphocytes; green, intravascular cancer and yellow, normal gland. Scale bars, 500 µm.

higher expression in the corresponding Visium cluster (Fig. 2a). Unsupervised denoising and imputation methods have been developed to account for the intrinsic sparsity of single-cell transcriptomics and ATAC-seq data that improve visualization and feature-to-feature correlation[17,18]. We applied a denoising deep count autoencoder (DCA) to our spatial ATAC and Visium datasets[18], which increased the signal-to-noise ratio in feature visualizations while preserving clustering structure (Extended Data Fig. 6). Accessibility at gene loci correlated with gene expression across anatomical structures (Extended Data Fig. 7). To identify putative regulatory elements underlying spatial patterns of gene expression, we performed peak co-accessibility analyses for differentially accessible gene loci. With this strategy, we identified 6,000 individual distal regulatory elements whose accessibility correlated to gene expression across tissues (Extended Data Fig. 8) and agreed with enhancer reporter assays (Extended Data Fig. 7c–e). To gain further insight into regulatory programs underlying gene expression, we performed motif enrichment analysis on these cluster-specific distal peaks. We found that the most enriched motifs in central nervous system clusters corresponded to well-characterized proneural transcription factors (for example, Neurog1, Neurod1, Ascl1). Conversely, motifs enriched in mesenchymal regulatory elements corresponded to factors known to be involved in bone and muscle development (for example, Smad3, Twist1, Myog), while liver-specific distal regulatory elements were highly enriched in binding sites for Tal1 and Gata transcription factors, consistent with their role in hematopoiesis (Extended Data Fig. 8d).

To evaluate whether spatial ATAC could identify regulatory programs underlying lineage differentiation within a developing tissue, we focused on the cerebral cortex at E15.5, a well-characterized structure in which SOX2+ progenitors in the subventricular zone generate neurons

that migrate to upper cortical layers[19]. Based on SOX2 immunostaining, we selected progenitor- and neuron-rich spots and performed motif enrichment on the top differentially accessible peaks (Fig. 2d–f). We identified cortical progenitor (for example, Sox2, Lhx2, Emx1) and neuronal (for example, Neurog1, Cux2) transcription factors among the top enriched motifs in the respective clusters (Fig. 2f). Further, we could link regulatory elements to the nearest genes that showed the corresponding patterns of layer-specific gene expression, and gene accessibility correlated with expression in the respective cortical layer (Fig. 2g,h). Next, we integrated the cortical spatial ATAC spots with single-cell RNA-sequencing (scRNA-seq) data from the same developmental stage[20]. Using the integrated dataset, we calculated pseudotime scores along the neuronal differentiation trajectory, which aligned single cells and spatial ATAC spots and recapitulated the inside-out differentiation trajectory of the developing cortex (Fig. 2i–j).

Finally, we applied spatial ATAC to human breast cancer, a tumor type of widespread public health concern in which pathological classification informs therapy decisions[21]. We profiled adjacent sections using Visium and spatial ATAC. Spatial ATAC clustering and marker expression aligned with pathologist annotations, agreed with Visium clustering and could readily identify HER2-positive regions, their associated non-coding region accessibility and the presence of myeloid cells in the immediate tumor microenvironment (Fig. 2k–m and Extended Data Figs. 9 and 10).

Our spatial ATAC platform is readily implementable through common laboratory workflows and offers the possibility for integration with other existing and future 'omics' modalities. We envision that spatial ATAC will enable spatial non-coding functional genomics, while being instrumental in the identification of regulatory elements for specific cell targeting in gene therapy and the study of gene regulatory networks in development and disease.

Online content

Any methods, additional references, Nature Portfolio reporting summaries, source data, extended data, supplementary information, acknowledgements, peer review information; details of author contributions and competing interests; and statements of data and code availability are available at https://doi.org/10.1038/s41587-022-01603-9.

References

1. Nitzan, M., Karaiskos, N., Friedman, N. & Rajewsky, N. Gene expression cartography. *Nature* **576**, 132–137 (2019).
2. Klemm, S. L., Shipony, Z. & Greenleaf, W. J. Chromatin accessibility and the regulatory epigenome. *Nat. Rev. Genet.* **20**, 207–220 (2019).
3. Shen, Y. et al. A map of the *cis*-regulatory sequences in the mouse genome. *Nature* **488**, 116–120 (2012).
4. Corces, M. R. et al. The chromatin accessibility landscape of primary human cancers. *Science* **362**, eaav1898 (2018).
5. Ge, Y. et al. Stem cell lineage infidelity drives wound repair and cancer. *Cell* **169**, 636–650.e14 (2017).
6. Satpathy, A. T. et al. Massively parallel single-cell chromatin landscapes of human immune cell development and intratumoral T cell exhaustion. *Nat. Biotechnol.* **37**, 925–936 (2019).
7. Ma, S. et al. Chromatin potential identified by shared single-cell profiling of RNA and chromatin. *Cell* **183**, 1103–1116. e20 (2020).
8. Chen, S., Lake, B. B. & Zhang, K. High-throughput sequencing of the transcriptome and chromatin accessibility in the same cell. *Nat. Biotechnol.* **37**, 1452–1457 (2019).
9. Palla, G., Fischer, D. S., Regev, A. & Theis, F. J. Spatial components of molecular tissue biology. *Nat. Biotechnol.* **40**, 308–318 (2022).
10. Thornton, C. A. et al. Spatially mapped single-cell chromatin accessibility. *Nat. Commun.* **12**, 1274 (2021).
11. Deng, Y. et al. Spatial profiling of chromatin accessibility in mouse and human tissues. *Nature* **609**, 375–383 (2022).
12. Buenrostro, J. D., Giresi, P. G., Zaba, L. C., Chang, H. Y. & Greenleaf, W. J. Transposition of native chromatin for fast and sensitive epigenomic profiling of open chromatin, DNA-binding proteins and nucleosome position. *Nat. Methods* **10**, 1213–1218 (2013).
13. Ståhl, P. L. et al. Visualization and analysis of gene expression in tissue sections by spatial transcriptomics. *Science* **353**, 78–82 (2016).
14. Preissl, S. et al. Single-nucleus analysis of accessible chromatin in developing mouse forebrain reveals cell-type-specific transcriptional regulation. *Nat. Neurosci.* **21**, 432–439 (2018).
15. Stuart, T., Srivastava, A., Madad, S., Lareau, C. A. & Satija, R. Single-cell chromatin state analysis with Signac. *Nat. Methods* **18**, 1333–1341 (2021).
16. Bergenstråhle, J., Larsson, L. & Lundeberg, J. Seamless integration of image and molecular analysis for spatial transcriptomics workflows. *BMC Genomics* **21**, 482 (2020).
17. Li, Z. et al. Chromatin-accessibility estimation from single-cell ATAC-seq data with scOpen. *Nat. Commun.* **12**, 6386 (2021).
18. Eraslan, G., Simon, L. M., Mircea, M., Mueller, N. S. & Theis, F. J. Single-cell RNA-seq denoising using a deep count autoencoder. *Nat. Commun.* **10**, 390 (2019).
19. Greig, L. C., Woodworth, M. B., Galazo, M. J., Padmanabhan, H. & Macklis, J. D. Molecular logic of neocortical projection neuron specification, development and diversity. *Nat. Rev. Neurosci.* **14**, 755–769 (2013).
20. La Manno, G. et al. Molecular architecture of the developing mouse brain. *Nature* **596**, 92–96 (2021).
21. Wu, S. Z. et al. A single-cell and spatially resolved atlas of human breast cancers. *Nat. Genet.* **53**, 1334–1347 (2021).

Publisher's note Springer Nature remains neutral with regard to jurisdictional claims in published maps and institutional affiliations.

Open Access This article is licensed under a Creative Commons Attribution 4.0 International License, which permits use, sharing, adaptation, distribution and reproduction in any medium or format, as long as you give appropriate credit to the original author(s) and the source, provide a link to the Creative Commons license, and indicate if changes were made. The images or other third party material in this article are included in the article's Creative Commons license, unless indicated otherwise in a credit line to the material. If material is not included in the article's Creative Commons license and your intended use is not permitted by statutory regulation or exceeds the permitted use, you will need to obtain permission directly from the copyright holder. To view a copy of this license, visit http://creativecommons.org/licenses/by/4.0/.

© The Author(s) 2023

https://doi.org/10.1038/s41587-022-01603-9

Methods

Animal tissue processing

Time pregnant C57BL/6 mice were purchased from Janvier and were euthanized by cervical dislocation at embryonic day 12.5, 13.5 or 15.5 for embryo harvesting. All experimental procedures were carried out in accordance with the Swedish and European Union guidelines and approved by the local committee for ethical experiments on laboratory animals in Sweden (Stockholms Norra Djurförsöksetiska Nämnd) under ethical permit numbers N155/16 and 20785/2020.

The tissues were harvested on ice-cold PBS and snap frozen in optimal cutting temperature compound (Tissue-Tek, 4583) blocks in a dry ice-isopentane bath at −60 °C and stored at −80 °C until being sectioned.

Collection of tumor samples from patients with breast cancer

Breast cancer tissues were obtained from the Department of Clinical Pathology and Cancer Diagnostics at Karolinska University Hospital, Stockholm, Sweden. Experimental procedures and protocols were approved by the regional ethics review board (Etikprövningsnämnden) in Stockholm (2016/957-31, amendments 2017/742-32 and 2021-00795), and informed consent was obtained from the participating patient.

The samples were obtained from a breast tumor removed from a patient with treatment-naive invasive ductal carcinoma. The tumor was divided into several regions and collected freshly by a pathologist depending on the size of the tumor. From each region, tissue was isolated for direct embedding in optimal cutting temperature compound, followed by immediate freezing and storage at −80 °C until further analysis. Histological evaluations of the patient's tumor were performed by pathologists for diagnostic purposes: tumor characteristics, including grade, size, hormone receptor, HER2 and KI67 status are presented in Supplementary Table 3.

Spatial ATAC

Cryosections were cut on a cryostat (Leica, NX70) at a 10 µm thickness and placed on spatially barcoded OMNI glass slides (10X Genomics). In brief, each OMNI array slide contained eight capture areas, each covered by 5,000 barcoded spots with diameters of 55 and 100 µm between spots. Each spot contained millions of DNA oligonucleotides encoding a 16 nt spatial barcode, serving as *x* and *y* coordinates, a PCR handle for library amplification, a 12-nt unique molecular identifier and a 7-nt generic capture sequence used for splint oligonucleotide hybridization (Supplementary Table 1). Slides were first heated at 37 °C for 1 min to adhere the tissue to the slide. Then, the sections were crosslinked in freshly prepared methanol-free 0.5% formaldehyde (Polysciences, 18814) diluted in Dulbecco's PBS (DPBS) for 10 min at room temperature, followed by rinsing in 500 mM Tris-HCl pH 8 (Thermo, AM9856) to quench the formaldehyde. After dipping the slide in DPBS three times, the sections were immunostained as follows: the tissue sections were blocked by incubation for 5 min with staining buffer (DPBS containing 5% Donkey serum, 0.1% NP-40 (Thermo 28324) and 0.005% Digitonin (Promega G9441)). The staining buffer was then removed, and the primary antibody dilution added (antibodies used were: rabbit anti-SOX2 Merck 5603, 1:100; goat anti-SOX9 R&D 3075, 1:300 and antinuclear antigen Novus 235-1, 1:100) and incubated at room temperature for 30 min. Then, washing was performed twice with staining buffer for 3 min each, followed by addition of donkey anti-rabbit or anti-goat Alexa 647-conjugated IgG secondary antibodies (Thermo 31573 or 21447; 1:500), and incubation at room temperature for 15 min. Then, washing was performed three times with staining buffer for 3 min each and finally pipette-washed with DPBS once. The slides were then spin dried, covered with 85% glycerol, mounted with a coverslip and imaged in a Zeiss LSM 700 (×10 magnification) confocal or in a Metafer VSlide system (×20 magnification) epifluorescence microscope to record tissue coordinates and capture area fiducials. The images were processed with the VSlide software (v.1.0.0) or with Fiji (v.2.3.0)[22].

After image acquisition, the glycerol was removed by dipping in DPBS and a layer of isopropanol was then added to the arrays, decanted and air-dried. The slide was then rehydrated in DPBS followed by ATAC permeabilization (0.01% digitonin, 0.1% Tween-20, 0.1% NP-40, 10 mM Tris-HCl pH 7.4, 10 mM NaCl, 3 mM $MgCl_2$) at room temperature for 10 min.

Custom Tn5 transposomes (30 µM) were assembled using Nextera adapter oligonucleotides A and B (Supplementary Table 1) according to ref. 23. Tagmentation was performed according to OMNI ATAC-seq[24] at 37 °C for 1 h under gentle shaking (300 rpm every 5 min) using 2 µl Tn5 in tagmentation mix (25 µl 2× TD buffer, 16.5 µl DPBS, 0.5 µl 1% digitonin, 0.5 µl 10% Tween-20). To stop the tagmentation and strip the transposase from DNA, sections were incubated with 50 mM EDTA while ramping down to 30 °C for 10 min. To hybridize the tagments to the barcoded surface oligonucleotides, we then incubated the sections with a 2 µM solution of splint oligonucleotide (in 3× SSC buffer containing 0.01% Triton-X100, 0.8 µg $µl^{-1}$ Proteinase K and 2.5% PEG8000) overnight at 30 °C. Next, the sections were rinsed in 2× NEB 2.1 buffer, and subsequently incubated with ligation and polymerization solution (1× NEB 2.1 containing 3 U of T4 DNA polymerase, 2,000 U of T4 DNA ligase, 100 µM dNTPs, 1 mM ATP, all from NEB) and incubated at 18 °C for 4 h. Tissue removal was then performed using 2 mg ml^{-1} Proteinase K in PKD-buffer (Qiagen), and incubated at 56 °C for 30 min (shaking at 300 rpm). The slides were then sequentially washed in 2× SSC 0.1% SDS, 0.2× SSC and 0.1× SSC and finally spin dried.

Library preparation and sequencing

Spatially barcoded single-stranded DNA fragments were released from the surface by denaturation with 0.08 M KOH at room temperature for 10 min and then quenched in 10 µl of 1 M Tris pH 7. The denatured fragments were pH adjusted with sodium acetate and cleaned with MinElute Reaction Cleanup Kit (Qiagen, 28204). The eluted DNA was then amplified using PCR using Partial.R1 and Ad2.short oligonucleotides for 15 cycles using PrimeSTAR Max DNA Polymerase mix (Takara, R045B). The amplified products were purified using 0.9× SPRI beads and i7-indexed in a second PCR (four cycles) using PE1.0 and Ad2.X (where X is the sample index from ref. 12) oligonucleotides and KAPA HiFi HotStart Mix (Roche, KK2602). The final indexed libraries were cleaned up using 0.8× SPRI beads and adjusted to the desired molarity based on the concentrations measured using Qubit HS double-stranded DNA Assay Kit (Thermo, Q32854) and the average fragment size from HS DNA Bioanalyzer kit (Agilent, 5067-4626).

Pooled libraries were then sequenced on Illumina Nextseq 550 or 2000 instrument using custom sequencing oligonucleotides for Read1 and Index2 (CustomR1 and CustomI2). We sequenced 65 bases for reads 1 and 2 (genomic sequence), 28 bases for i5 (spatial barcode and unique molecular identifier) and eight bases for i7 (sample index). All DNA oligonucleotides are listed in Supplementary Table 1.

H&E staining

Tissue sections from breast cancer specimens were first dried with isopropanol (Fisher Scientific, A461-1) before staining. The sections were then stained with Mayer's hematoxylin (Agilent, S3309) for 4 min, washed in ultrapure water, incubated in bluing buffer (Agilent, CS702) for 2 min, washed in Milli-Q water and further incubated for 1 min in 1:20 eosin solution (Sigma-Aldrich, HT110216) in Tris-buffer (pH 6). The tissue sections were dried for 5 min at 37 °C and then mounted with 85% glycerol (Merck, 104094) and a coverslip. Imaging was performed using the Metafer VSlide system at ×20 magnification.

Data preprocessing

Raw reads were preprocessed using 10X Genomics' CellRanger ATAC pipeline (v.2.0.0). We used a custom 'barcode_whitelist' specifying positional barcodes from the spatial arrays and default reference genomes (mm10, v.2.0.0 for the mouse data and hg38, v.2.0.0 for the human

data). All other parameters for 'mkfastq' and 'count' functions were set to default. Sequencing data from each section was processed separately and subsequently integrated with Seurat (v.4.1.0, ref. 25) and Harmony (v.0.1.0, ref. 26) R packages (below).

Analysis and visualization

For the embryos, we assayed sections across different developmental stages and integrated them for downstream analysis. To do so, we first obtained age-specific fragment files from ENCODE[27] and merged them using GenomicRanges's (v.1.46.1, ref. 28) 'reduce()' function. We then used these to create new accessibility matrices with a common set of 269,767 peaks. For comparison, we also called peaks on the merged dataset using MACS2 (v.2.2.6), as well as constructed feature matrices from 5 kb genomic bins, and inspected the clustering concordance across pre-processing strategies. Peak-barcode matrices for the human breast cancer sample were constructed using a set of 215,978 peaks from ref. 4. We next subset the matrices to only include spots overlaying tissue, which were manually identified in Loupe Browser (v.6.0.0) after aligning immunofluorescence pictures with capture area fiducials. Loupe browser was also used to select SOX2+ and SOX2− cortical spots in two mouse E15.5 sections. The spatial object was created using STutility R package (v.0.1.0, ref. 16), using tissue spot coordinates adjusted for the dimensions of the microscope images. STutility was used to produce the spatial plots using 'ST.FeaturePlot()' function for quantitative variables. TSS enrichment plots and FragmentHistograms were generated using ArchR (v.1.0.1)[29].

For each tissue type, we merged sections and performed normalization and dimensionality reduction on all peaks using Signac's (v.1.6.0, ref. 15) 'RunTFIDF()' and 'RunSVD()' functions with default settings. We calculated gene activity using Ensembl annotations (EnsDb.Mmusculus.v79, v.2.99.0 and EnsDb.Hsapiens.v86, v.2.99.0), followed by log-normalization and principal component analysis. Genes from the *Pcdh* and *Ugt* gene clusters were removed from the gene activity assay before downstream analysis. For the embryos, graph clustering and UMAP were then performed on the peaks assay after integrating section-wise with Harmony on the top seven dimensions and at a resolution of 0.7, which enabled identification of clusters that reflect the underlying anatomical structures. Human breast cancer sections, which were obtained from the same tissue specimen, were merged directly using Seurat's 'merge()' function followed by UMAP and graph clustering on dimensions 2 to 7, and at a resolution of 0.5. Cluster-wise Spearman's correlation of the chromatin accessibility profile was calculated for peaks around the transcription start site (that is, between −1,000 bp and +100 bp from TSS position) and for distal elements, using GenomicRanges's GetTSSPositions() followed by Signac's ClosestFeature() functions to annotate the peaks, and Seurat's 'AverageExpression()' to obtain cluster-wise average accessibility levels for each peak. Differential accessibility analysis was carried out on peaks using Seurat's FindAllMarkers() function with method = 'LR' and unique fragments as the latent variable, and with logfc.threshold = 0.2 and min.pct = 0.01 to account for the sparsity of ATAC-seq data. FindAllMarkers() was also ran on the gene activity data with Wilcoxon's Rank Sum test and followed by Gene Ontology analysis using gprofiler2 R package (v.0.2.1). Differentially accessible features were retained at an adjusted P value of 0.05 after Bonferroni's correction. Co-accessible peaks were identified after running LinkPeaks() on differentially accessible genes with a correlation cut-off, as well as a minimum 1 kb distance from the TSS. Motif enrichment analysis was carried out using FindMotifs() function and a set of clustered motifs from ref. 30 on all linked peaks. Non-redundant top motifs were highlighted. For motif enrichment analyses in the developing mouse cortex, we first ran FoldChange() on peaks from SOX2+ and SOX2− cortical spots and then selected the top 500 peaks for motif analyses as above. Full lists of enriched motifs are provided in Supplementary Table 2. Vista enhancers were downloaded from https://enhancer.lbl.gov/ and genome coordinates were lifted to mm10 using the UCSC liftover tool before intersection with spatial ATAC tissue-specific peaks using bedtools (v.2.19.0)[31].

Denoising

Using a DCA (v.0.3.4, ref. 18), we denoised the peak-barcode matrix of the combined objects, as well as the gene activity matrices. For the peaks data, we specified the following parameters: –nosizefactors –nonorminput –nologinput, whereas DCA was run with default settings on the gene activity data. Additionally, we performed DCA with default parameters on Visium data from the mouse embryo and human breast cancer (below). Dimensionality reduction and clustering was performed on the denoised data as above to evaluate concordance between original and denoised data. While clustering and differential accessibility analysis were conducted on original data, denoised data was used for visualization of accessibility levels and for multimodal integration with single-cell data (below).

Spatial analysis

STutility's RunNMF() function was run with 'nfactors = 8' after ordering the top 25% variable features according to spatial correlation. Harmony integration on tissue section and graph clustering was performed using non-negative matrix factorization factors in dimensionality reduction and the groups obtained this way were compared with the spatial-agnostic clusters obtained with the original peaks assay.

snATAC-seq

To analyze spatial ATAC datasets in conjunction with snATAC-seq, we prepared single nuclei suspensions from fresh frozen embryos (E12.5, E13.5 and E15.5) that were littermates to those used for spatial ATAC. Three to five 70 µm frozen sections were obtained for each embryonic stage matching the anatomical landmarks from spatial ATAC sections. Frozen sections were then dissociated according to the 10X Chromium Single Nuclei Isolation kit (1000494) omitting the debris removal step to avoid cell loss. Nuclei suspensions were stained with 7-AAD (Miltenyi; 1:50) and sorted on a BD Fusion flow cytometer with a 100 µm nozzle. Nuclei were then immediately processed according to the 10X Genomics' Single Cell ATAC Next GEM kit (v.1.1). Sequencing data were demultiplexed and mapped using CellRanger ATAC with default parameters yielding a total of 1,879 cells. Accessibility matrices were constructed with Signac's FeatureMatrix() function using the ENCODE peak set to enable direct comparison with the spatial data. Single-nucleus data were subsequently integrated with the spatial profiles using FindIntegrationAnchors() with 'rlsi' reduction, followed by IntegrateEmbeddings() and RunHarmony() with sample of origin as grouping variable, which was used to obtain UMAP visualizations of the co-embedded data. The concordance of spatial and single-nucleus chromatin accessibility data was subsequently explored by cluster-wise correlation analysis of all peaks and gene bodies that were log-transformed and normalized to adjust for sequencing depth. Differential accessibility testing for gene activities was used for cluster annotation using ref. 17 for reference. Furthermore, we mapped the clusters resulting from integration onto the spatial ATAC sections to confirm the validity of our annotations.

We further analyzed our spatial ATAC data together with published snATAC-seq profiles of forebrain development sampled at the same developmental stages (that is, E12.5, E13.5 and E15.5). For this purpose, we constructed accessibility matrices from the snATAC-seq[10] data using the ENCODE peaks set, and using the Loupe Browser we subset the spatial ATAC profiles to only include capture spots overlaying the forebrain. Next, we integrated the multimodal data as above and calculated prediction scores on the spatial data for each of the clusters in the snATAC-seq profiles (that is, by means of Signac's TransferData() function).

Visium

The 10X Genomics' Visium platform was used to obtain spatial transcriptomics data for tissue samples matching our spatial ATAC sections (that is, either on consecutive tissue slices from breast tumor block or on similar sagittal level of embryos from the same litter).

Raw data were pre-processed using SpaceRanger's (v.1.3.1) mkfastq and count functions with default parameters, and the resulting gene-barcode matrices were then analyzed with Seurat for normalization, dimensionality reduction and clustering, and with STUtility for plotting. Visium data were denoised with DCA and default parameters for visualizations and comparison with spatial ATAC data.

Integrative multimodal analysis

We performed multimodal comparison of our spatial ATAC data using either spatial or single-cell transcriptomics. To measure cluster-wise concordance between gene expression and accessibility, we analyzed in parallel spatial ATAC and spatial RNA-seq data from the embryos and obtained cluster markers for each modality, which we used to calculate module scores (with Seurat's AddModuleScore()) in each assay. Furthermore, we aggregated clusters into anatomical structures and performed correlation analysis between expression and accessibility of all genes in the dataset.

Additionally, we performed multimodal integrative analysis between spatial ATAC and single-cell RNA-seq data. For the embryos, we obtained a developmental transcriptional atlas from ref. 20, and subset it to include cells from E15 brains. In parallel, we restricted our analysis of spatial chromatin data to the cortex of E15.5 mice and manually subset spots overlaying the region of interest. Specifically, we focused our analysis to only comprise the dorsal forebrain and specifically looked at cells in the neurogenic trajectory (that is, radial glia, intermediate progenitors and neurons). Single-cell data were processed according to Seurat's standard workflow and subset to $n = 1{,}500$ cells randomly sampled across the clusters. We integrated spatial ATAC and single-cell RNA-seq data using canonical correlation analysis and 2,000 anchor features. Co-embedded data were subsequently subjected to dimensionality reduction using principal component analysis. UMAP visualizations calculated on the top seven components were, finally, used to order cells in pseudotime using monocle3 (v.1.0.0, ref. 32) and the radial glia cluster as root cells.

For the human breast cancer data, we obtained a comprehensive single-cell RNA-seq atlas[21] and processed it with Seurat's standard workflow. We then probed enrichment of the main cell types in our spatial ATAC and spatial RNA-seq clusters. To do so, we adopted the author's classification of cells in the highest tier (that is, 'celltype_major') and used Seurat's label transfer workflow based on canonical correlation analysis to obtain prediction scores for each cell type in the single-cell dataset.

Reporting summary

Further information on research design is available in the Nature Portfolio Reporting Summary linked to this article.

Data availability

All raw data and processed count matrices from mouse tissues can be obtained at Gene Expression Omnibus using the accession code GSE214991 (ref. 33). Human sequencing data are stored in the SciLife Data Repository at https://doi.org/10.17044/scilifelab.21378279.v1 (ref. 34). Additionally, we analyzed previously published datasets, a list of which is provided in Supplementary Table 2.

Code availability

All analysis code used can be found at https://github.com/marzamKI/spatial_atac (ref. 35).

References

22. Schindelin, J. et al. Fiji: an open-source platform for biological-image analysis. *Nat. Methods* **9**, 676–682 (2012).
23. Picelli, S. et al. Tn5 transposase and tagmentation procedures for massively scaled sequencing projects. *Genome Res.* **24**, 2033–2040 (2014).
24. Corces, M. R. et al. An improved ATAC-seq protocol reduces background and enables interrogation of frozen tissues. *Nat. Methods* **14**, 959–962 (2017).
25. Hao, Y. et al. Integrated analysis of multimodal single-cell data. *Cell* **184**, 3573–3587.e29 (2021).
26. Korsunsky, I. et al. Fast, sensitive and accurate integration of single-cell data with Harmony. *Nat. Methods* **16**, 1289–1296 (2019).
27. Gorkin, D. U. et al. An atlas of dynamic chromatin landscapes in mouse fetal development. *Nature* **583**, 744–751 (2020).
28. Lawrence, M. et al. Software for computing and annotating genomic ranges. *PLoS Comput. Biol.* **9**, e1003118 (2013).
29. Granja, J. M. et al. ArchR is a scalable software package for integrative single-cell chromatin accessibility analysis. *Nat. Genet.* **53**, 403–411 (2021).
30. Vierstra, J. et al. Global reference mapping of human transcription factor footprints. *Nature* **583**, 729–736 (2020).
31. Quinlan, A. R. & Hall, I. M. BEDTools: a flexible suite of utilities for comparing genomic features. *Bioinformatics* **26**, 841–842 (2010).
32. Cao, J. et al. The single-cell transcriptional landscape of mammalian organogenesis. *Nature* **566**, 496–502 (2019).
33. Zamboni, M. & Llorens-Bobadilla, E. Developing mouse embryo. GSE214991 (Gene Expression Omnibus, 2022); https://www.ncbi.nlm.nih.gov/geo/query/acc.cgi?acc=GSE214991
34. Zamboni, M., Llorens-Bobadilla, E., Chen, X. & Hartman, J. Spatially resolved chromatin accessibility and transcriptomic profiling of human breast cancer (SciLifeLab Data Repository, 2022); https://doi.org/10.17044/scilifelab.21378279.v1
35. Zamboni, M. Spatial_atac (GitHub, 2022); https://github.com/marzamKI/spatial_atac
36. Liu, Q. et al. A novel HER2 gene body enhancer contributes to HER2 expression. *Oncogene* **37**, 687–694 (2018).

Acknowledgements

We thank A. Andersson for initial help and advice with the analyses. L. Larsson, M. Lukoseviciute and C. Engblom for helpful discussions. V. Kumar for help adapting CellRanger. P. Backhaus for help in embryo harvesting. G. Winberg, H. Lönnqvist, M. Hagemann-Jensen and R. Sandberg for help preparing Tn5 and access to NextSeq sequencing. We thank the National Genomics Infrastructure, Sweden for providing infrastructure support. The data were analyzed using resources provided by SNIC through the Uppsala Multidisciplinary Center for Advanced Computational Science (SNIC/UPPMAX). This work was supported by grants from the Swedish Research Council (J.F., P.L.S. and E.L.-B.), the Swedish Foundation for Strategic Research (E.L.-B.), the Strategic Research Programs in Neuroscience StratNeuro (E.L.-B.) and in Stem Cells and Regenerative Medicine at Karolinska Institutet StratRegen (J.F.), the Swedish Cancer Foundation (J.F.), the Knut and Alice Wallenberg Foundation (J.F.) and a SSMF Postdoctoral grant (M.Z.).

Author contributions

E.L.-B., J.F. and P.L.S. conceived the project. E.L.-B., M.Z., M.M. and N.B. performed the experiments. M.Z. and E.L.-B. conducted the analyses and visualizations. X.C. and J.H. provided cancer samples and pathology annotations. E.L.-B. wrote the manuscript with input from all the authors. J.F. and P.L.S. acquired funding and supervised the project.

Funding
Open access funding provided by Karolinska Institute.

Competing interests
E.L.-B., M.Z., M.M., N.B., J.F. and P.L.S. are scientific consultants to 10X Genomics, which holds intellectual property rights to the spatial technology. The remaining authors declare no competing interests.

Additional information
Extended data is available for this paper at https://doi.org/10.1038/s41587-022-01603-9.

Supplementary information The online version contains supplementary material available at https://doi.org/10.1038/s41587-022-01603-9.

Correspondence and requests for materials should be addressed to Enric Llorens-Bobadilla or Patrik L. Ståhl.

Peer review information *Nature Biotechnology* thanks Zhicheng Ji and the other, anonymous, reviewer(s) for their contribution to the peer review of this work.

Reprints and permissions information is available at www.nature.com/reprints.

https://doi.org/10.1038/s41587-022-01603-9

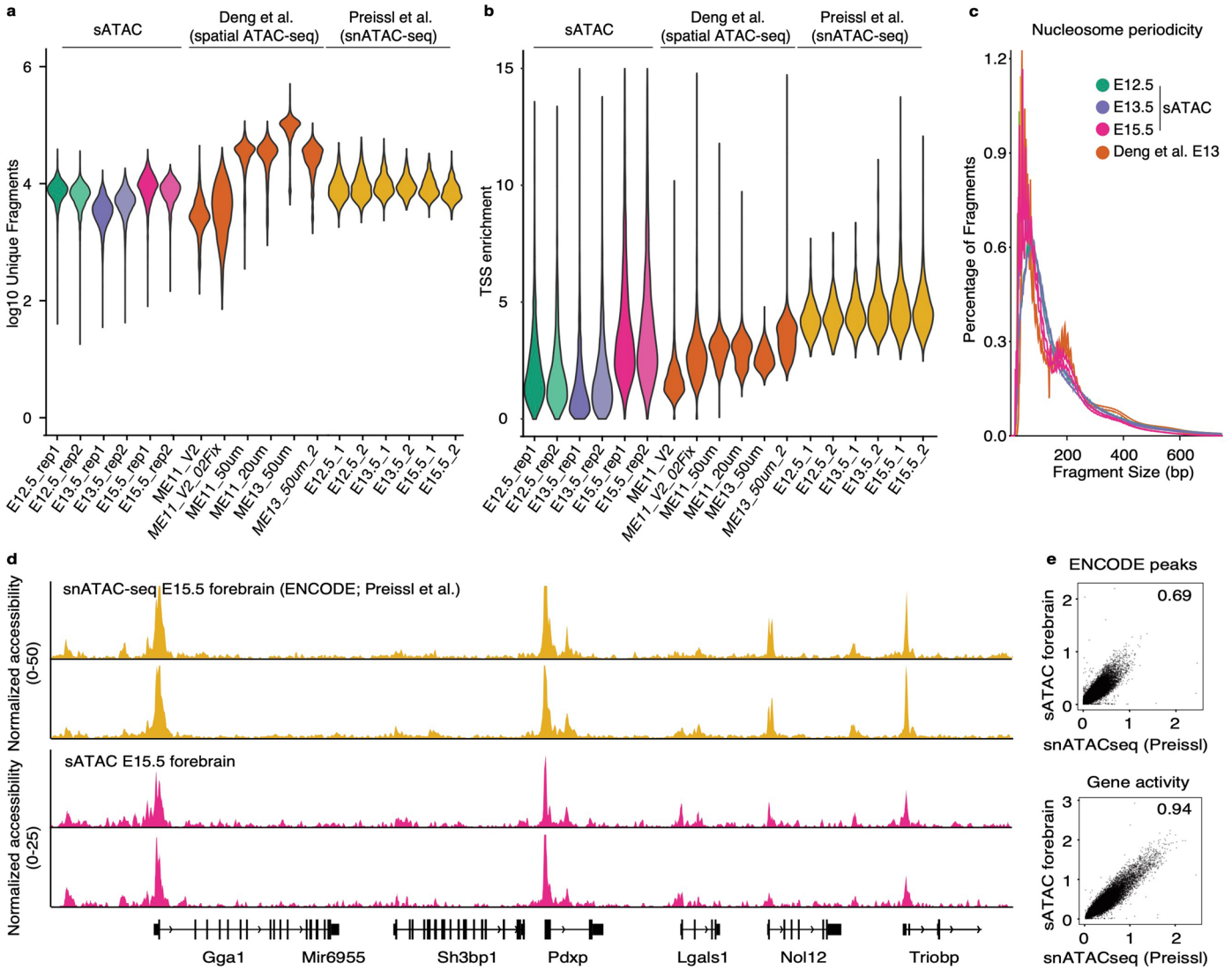

Extended Data Fig. 1 | Quality control metrics of spatial ATAC. a-b. Violin plot showing unique fragments per spot and TSS enrichment in embryo sections processed using spatial ATAC, spatial ATAC-seq from[10] and single-nucleus ATAC-seq from[14]. **c.** Fragment size histogram colored by technology and replicate as in Fig. 1b. **d.** Genome ATAC-seq coverage tracks from ENCODE E15.5 forebrain snATAC-seq replicates and aggregate signal from forebrain spots from two spatial ATAC E15.5 sections. **e.** Scatterplot showing the correlation (Spearman's rho) between log-normalized values for peak (top) and gene (bottom) accessibility for snATAC-seq and spatial ATAC mouse developmental forebrain datasets.

https://doi.org/10.1038/s41587-022-01603-9

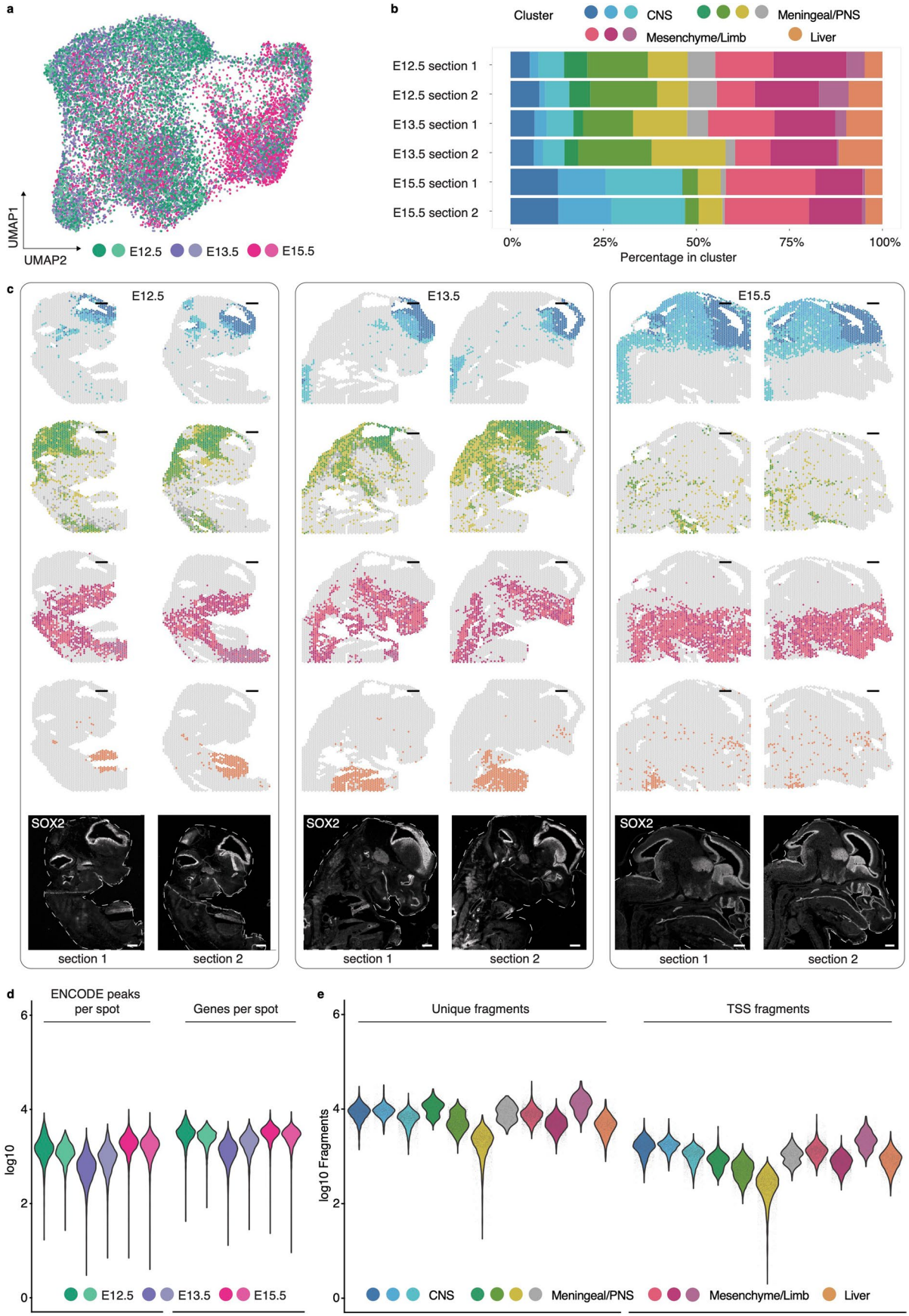

Extended Data Fig. 2 | spatial ATAC in mouse embryos. a. UMAP embedding corresponding to Fig. 1d colored by embryonic age and section replicate. **b**. Cluster proportions across embryo sections. **c**. Cluster families as in Fig. 1c for all sections analyzed (n = 6, 2 per embryonic stage). SOX2 immunostaining for the respective section at the bottom. Scale bars are 500 µm. **d**. Number of ENCODE peaks and genes detected per spot across sections. **e**. Numbers of unique fragments and TSS fragments across clusters. Each dot corresponds to a tissue spot.

https://doi.org/10.1038/s41587-022-01603-9

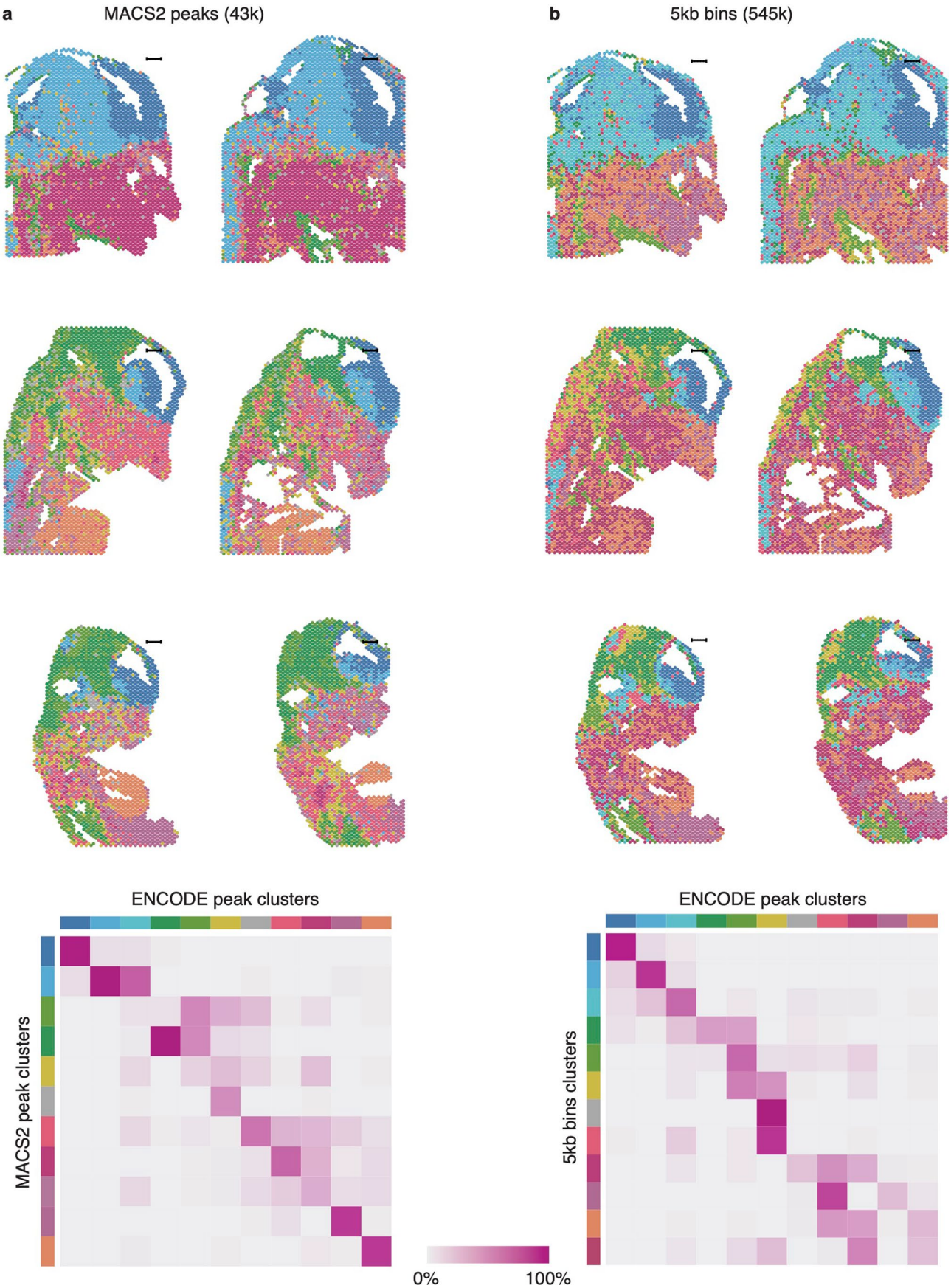

Extended Data Fig. 3 | spatial ATAC clustering robustness. a. Spatial ATAC clustering on E12.5, E13.5 and E15.5 replicate sections using peaks called by MACS2. Below, correspondence between cluster identities based on ENCODE peaks (Fig. 1c–g) or on MACS2 peaks. **b**. Same as in a, but using fragment counts in 5 kb genomic bins.

https://doi.org/10.1038/s41587-022-01603-9

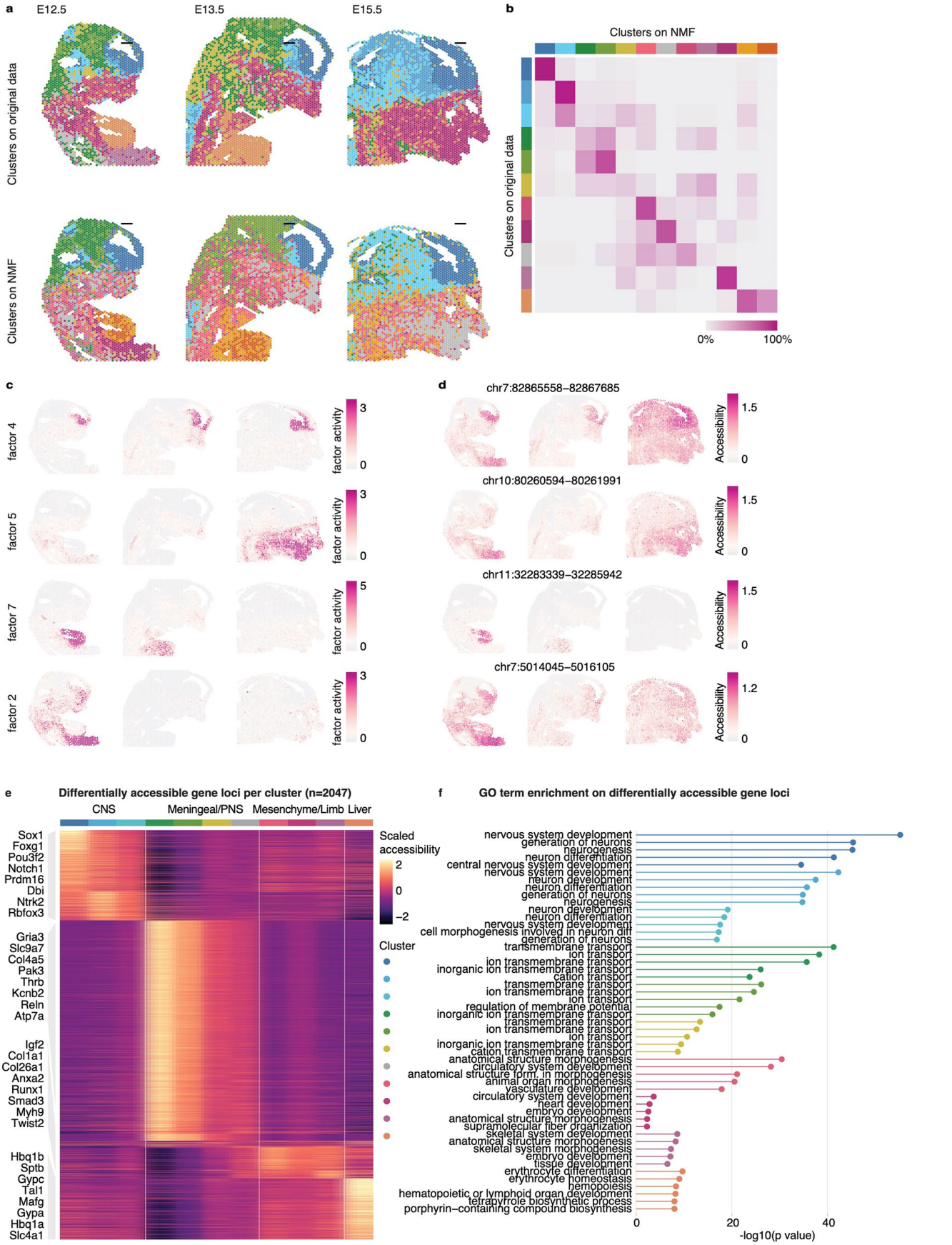

Extended Data Fig. 4 | See next page for caption.

https://doi.org/10.1038/s41587-022-01603-9

Extended Data Fig. 4 | Clustering of spatial ATAC data with spatially aware factor analysis, marker genes and gene ontology analysis. a. Spatial ATAC clusters based on LSI (top; sections and clusters from Fig. 1c shown again for comparison) or NMF (bottom) for dimensionality reduction. **b**. Heatmap displaying the percentage of spots assigned to LSI- or NMF-computed clusters. **c**. Spatial activity plots for selected factors enriched in forebrain, facial prominence, liver, and limb. **d**. Examples of the most contributing peaks for each factor represented in c. Scale bars are 500 µm. **e**. Heatmap showing scaled accessibility for the top differentially accessible genes (gene body + promoter) across clusters. Relevant markers are highlighted. **f**. Gene ontology enrichment analysis of the top marker genes colored by cluster. *P* values were determined with hypergeometric test followed by correction for multiple testing using g:Profiler's g:SCS algorithm.

https://doi.org/10.1038/s41587-022-01603-9

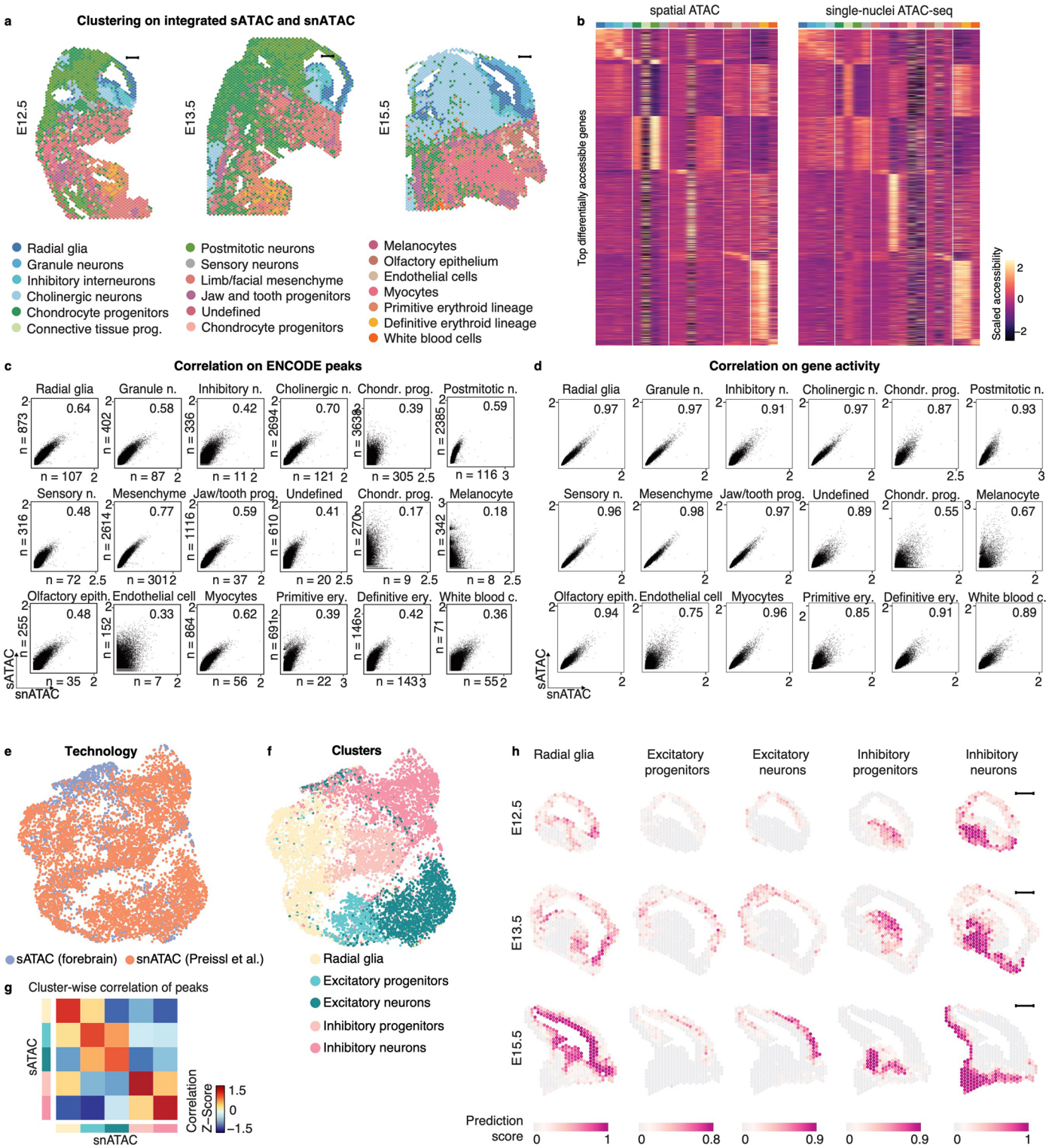

Extended Data Fig. 5 | Integration of spatial ATAC with single-nucleus ATAC-seq (snATAC-seq) during mouse development. a. Representative spatial ATAC sections with clustering based on integration with snATAC-seq data from the same developmental stages (clusters and colors consistent with Fig. 1j, k). **b**. Heatmaps showing scaled accessibility for differentially accessible gene loci (n = 2575) for all clusters across both technologies. **c**. Scatterplots comparing log-normalized accessibility at ENCODE peaks across clusters and technologies. Spearman's correlation coefficients are shown inside the plot and spot/cell numbers are reported in the respective axes. **d**. Same as in d but for log-normalized gene activity counts. **e**. UMAP embedding for spatial ATAC forebrain spots and age-matched snATAC-seq data from[14] colored by technology. **f**. UMAP embedding colored by cell identity according to Preissl et al. **g**. Heatmap depicting z-scored correlation coefficients for accessibility at ENCODE peaks across clusters and technologies. **h**. Prediction scores for snATAC-seq-defined cell clusters in f on spatial ATAC forebrain regions across developmental stages.

https://doi.org/10.1038/s41587-022-01603-9

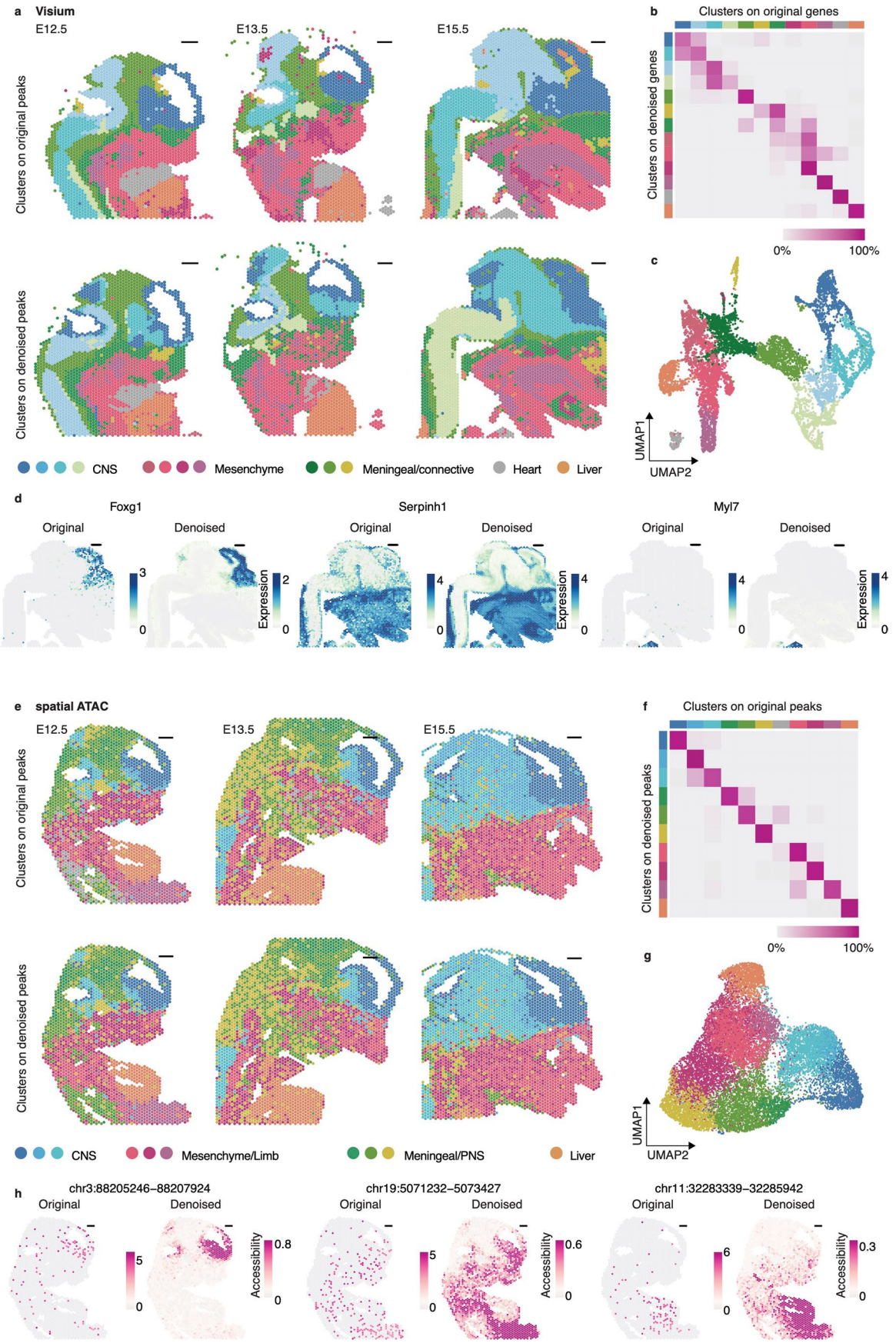

Extended Data Fig. 6 | See next page for caption.

https://doi.org/10.1038/s41587-022-01603-9

Extended Data Fig. 6 | Deep count autoencoder denoising of Visium and spatial ATAC. a. Visium clusters based on original (same as in Fig. 2a) or denoised gene counts. **b**. Heatmap displaying the percentage of spots being assigned to the clusters obtained from original or denoised Visium data. **c**. UMAP on denoised expression colored by cluster. **d**. Visualization of gene expression normalized counts before and after denoising on E15.5 sections. **e**. Clusters based on original or denoised spatial ATAC peak counts (same as in Fig. 1c, shown for comparison). **f**. Heatmap displaying the percentage of spots being assigned to the clusters obtained from original or denoised spatial ATAC data **g**. UMAP on denoised peaks colored by cluster. **h**. Visualization of normalized peak accessibility before and after denoising on E12.5 sections. Scale bars are 500 µm.

https://doi.org/10.1038/s41587-022-01603-9

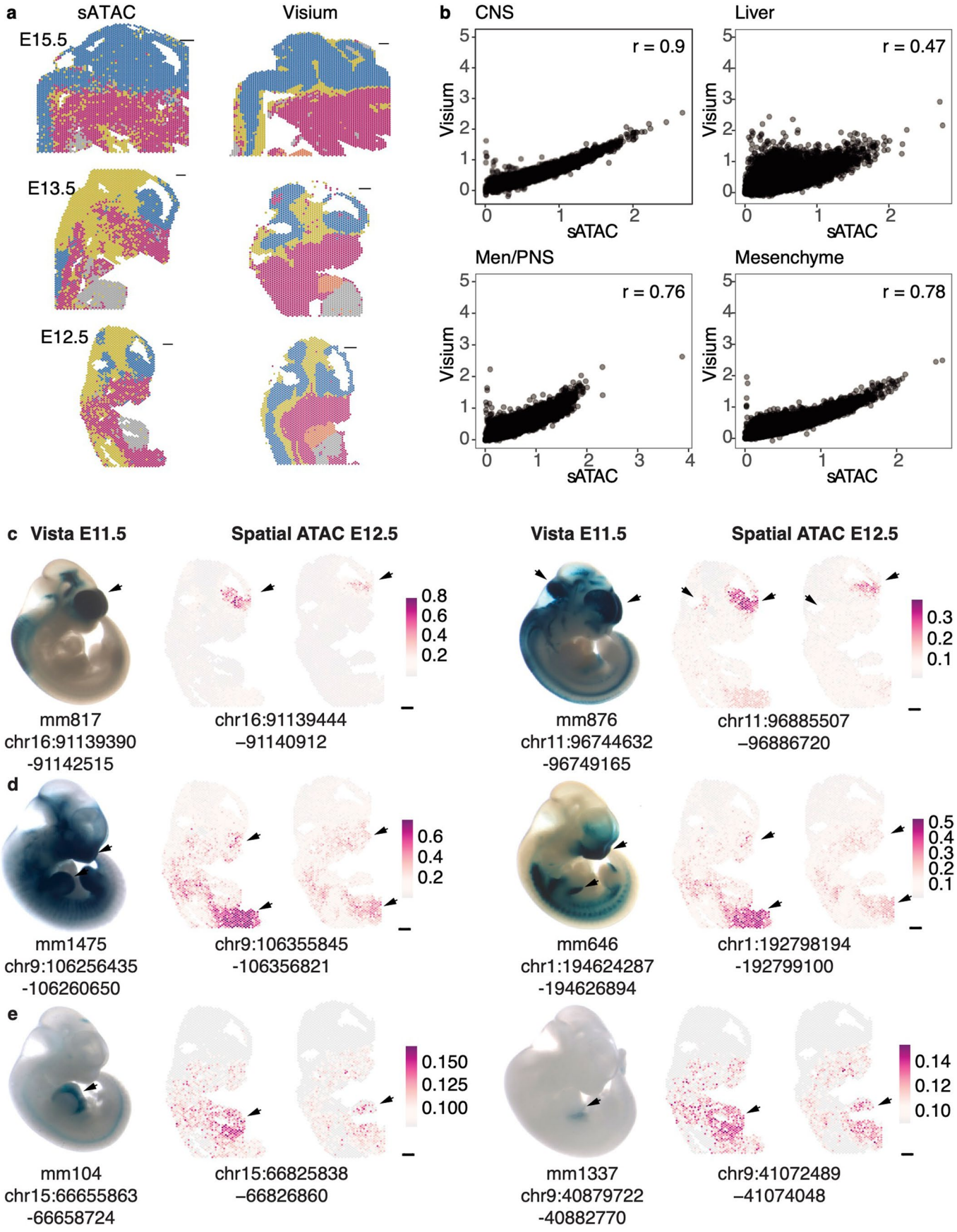

Extended Data Fig. 7 | See next page for caption.

https://doi.org/10.1038/s41587-022-01603-9

Extended Data Fig. 7 | Correlation between accessibility and expression and validation of spatial ATAC regulatory element accessibility. a. Spatial ATAC and Visium with clusters grouped according to the main anatomical structures common to the sections. **b**. Scatterplots showing the log-normalized counts for Visium gene expression and spatial ATAC gene activities across anatomical structures. Correlation coefficient is shown in the plot. **c**. Vista enhancer reporter expression for two CNS elements overlapping with differentially accessible spatial ATAC peaks. Genome coordinates under the Vista image according to mm9 genome assembly. Under spatial ATAC feature plots, mm10. **d**. Vista enhancer reporter expression for two liver elements overlapping with differentially accessible spatial ATAC peaks. **e**. Vista enhancer reporter expression for two limb elements overlapping with differentially accessible spatial ATAC peaks. Reporter images were obtained from https://enhancer.lbl.gov/. Scale bars are 500 µm.

https://doi.org/10.1038/s41587-022-01603-9

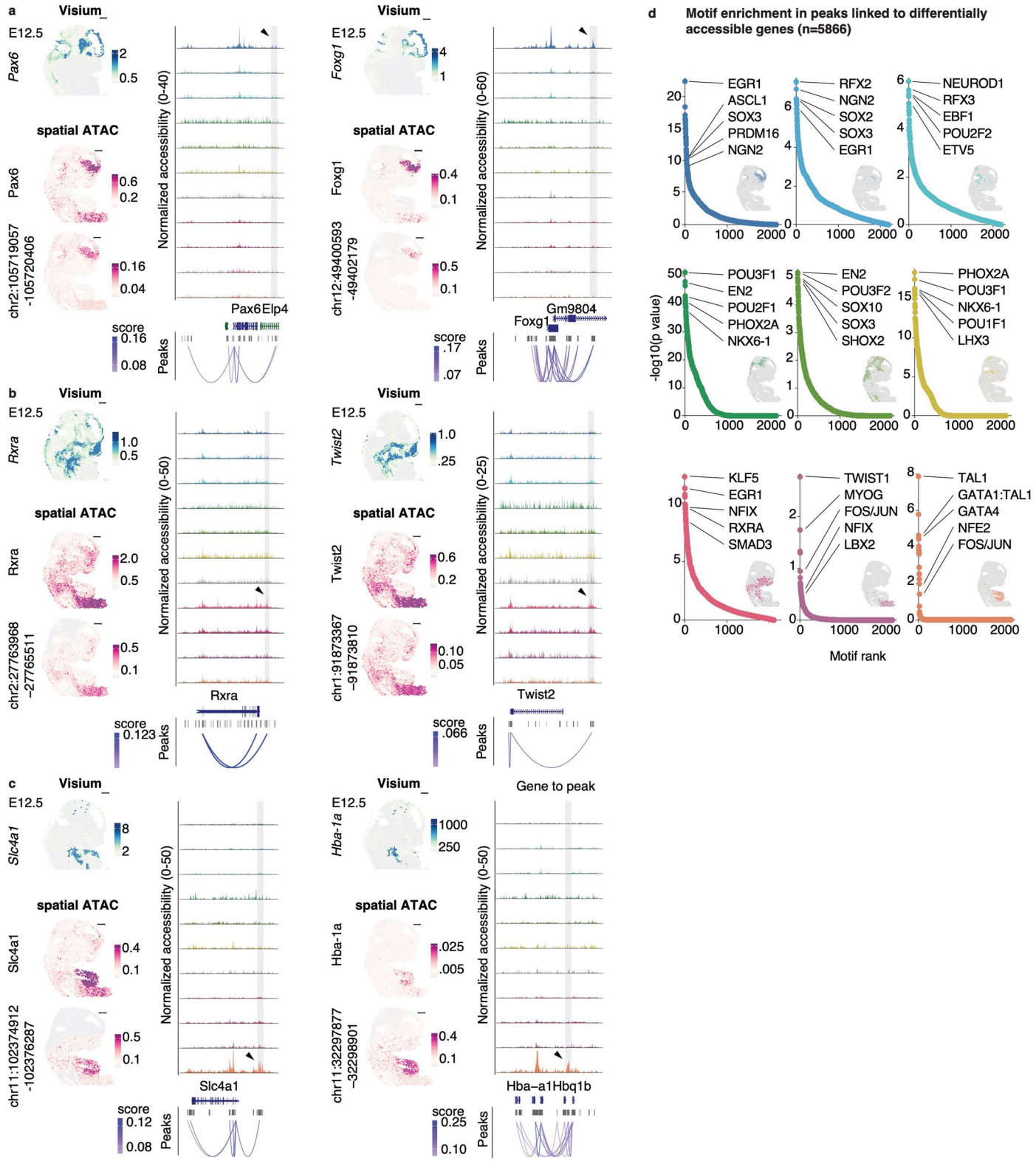

Extended Data Fig. 8 | Gene regulatory programs during mouse organogenesis. a. Visium expression, spatial ATAC gene activity and regulatory element accessibility at E12.5 for CNS/Forebrain markers Pax6 and Foxg1. The respective linked regulatory element is shown in gray. **b**. Visium expression, spatial ATAC gene activity and regulatory element accessibility for Mesenchyme/Limb markers Rxra and Twist2. The respective linked regulatory element is shown in gray. **c**. Visium expression, spatial ATAC gene activity and regulatory element accessibility for liver markers Slc4a1 and Hba-a1. The respective linked regulatory element is shown in gray. Arrowheads point to clusters for which the regulatory element is most accessible. **d**. Motif enrichment rank plots for cluster-specific distal elements. Selected top non-redundant transcription factor motifs are highlighted. *P* values were determined by a one-sided hypergeometric test. Scale bars are 500 µm.

https://doi.org/10.1038/s41587-022-01603-9

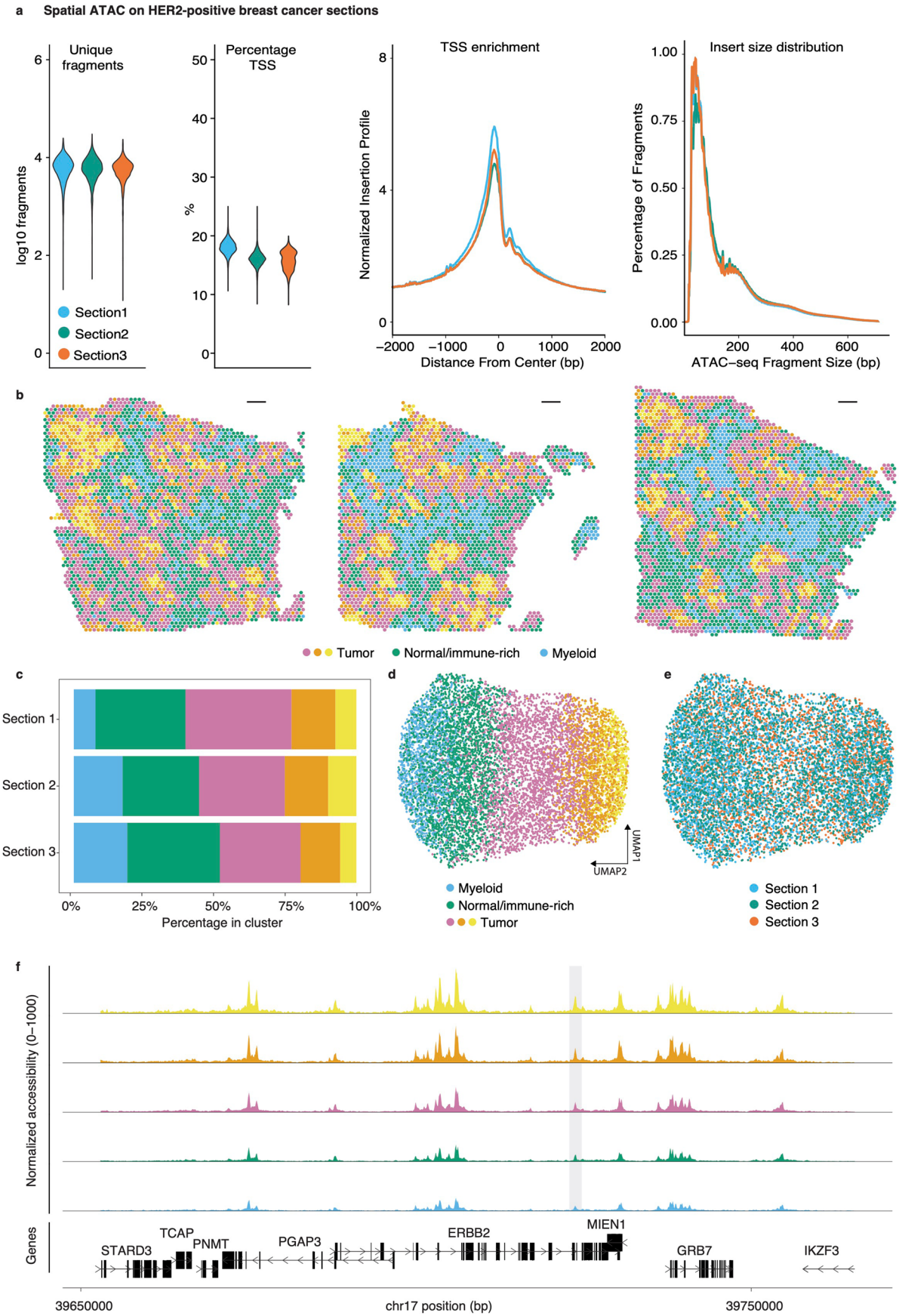

Extended Data Fig. 9 | See next page for caption.

https://doi.org/10.1038/s41587-022-01603-9

Extended Data Fig. 9 | Spatial ATAC on human HER2-positive breast cancer. **a**. On the left, violin plot showing unique fragments per spot and percentage TSS fragments in three adjacent sections processed using spatial ATAC. On the right, TSS enrichment and insert size distribution. **b**. Spatial ATAC clustering reveals tumor, immune-rich and normal tissue regions. **c**. Cluster percentage across sections. **d-e**. UMAP embedding on spatial ATAC peaks color-coded by cluster or tissue section. **f**. Genome tracks showing normalized spatial ATAC-seq fragment density around the HER2 (ERBB2) locus colored by cluster. The gray area marks a previously described gene body enhancer[36] shown in Fig. 2l. Scale bars are 500 μm.

https://doi.org/10.1038/s41587-022-01603-9

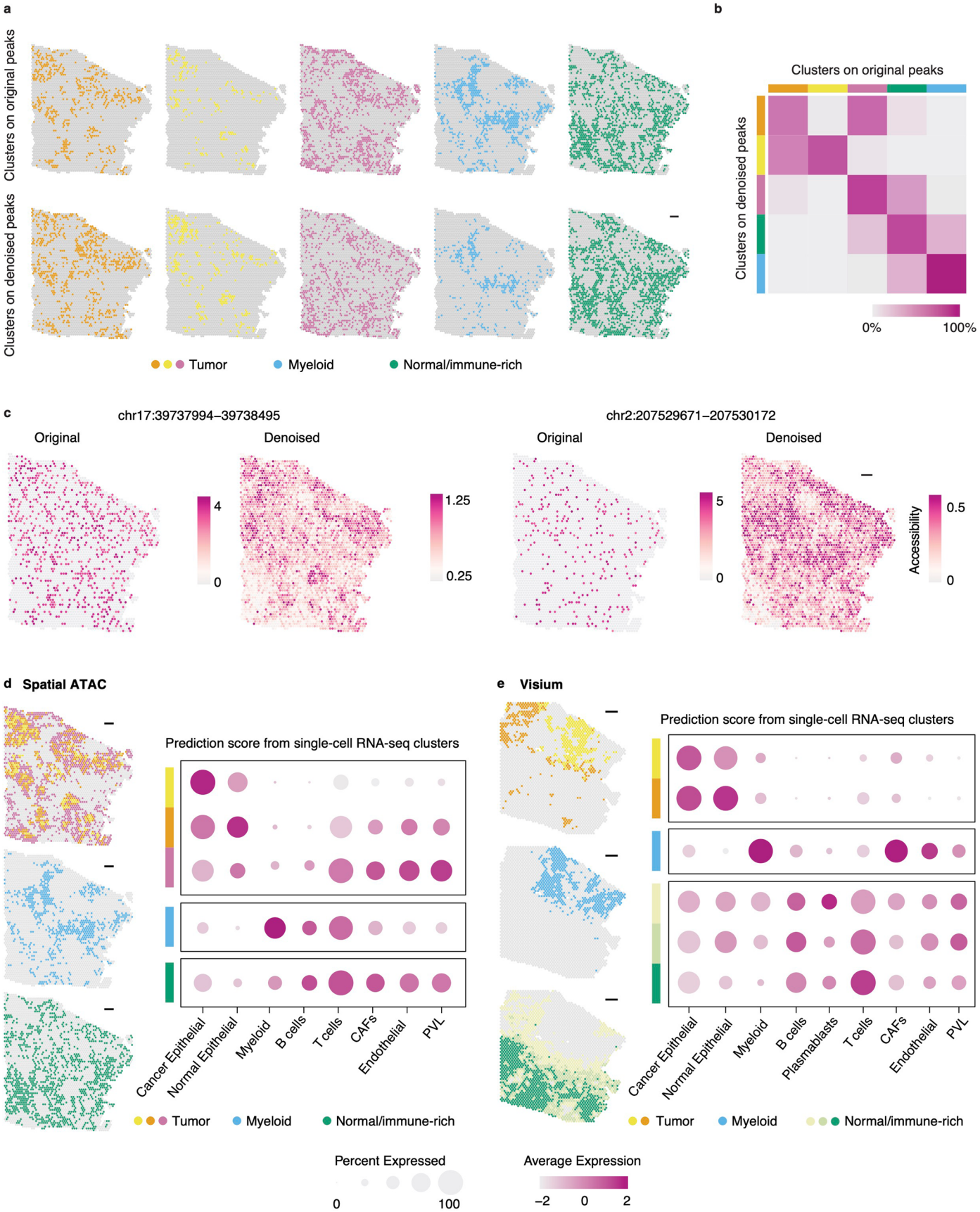

Extended Data Fig. 10 | See next page for caption.

https://doi.org/10.1038/s41587-022-01603-9

Extended Data Fig. 10 | Multimodal integration of single-cell RNA-seq with spatial ATAC and Visium on breast cancer sections. a. Clusters based on original or DCA denoised peak counts. **b**. Heatmap displaying the percentage of spots being assigned to the clusters obtained from original or denoised spatial ATAC data. **c**. Visualization of peak accessibility scores before and after denoising on one example section. **d**. Prediction scores from scRNA-seq signatures in spatial ATAC clusters reveal cell composition differences across clusters. **e**. Prediction scores from scRNA-seq signatures in Visium clusters. Scale bars are 500 µm.

nature research

Corresponding author(s): Enric Llorens-Bobadilla
Patrik L Ståhl

Last updated by author(s): 2022/11/04

Reporting Summary

Nature Research wishes to improve the reproducibility of the work that we publish. This form provides structure for consistency and transparency in reporting. For further information on Nature Research policies, see our Editorial Policies and the Editorial Policy Checklist.

Statistics

For all statistical analyses, confirm that the following items are present in the figure legend, table legend, main text, or Methods section.

n/a	Confirmed
☐	☒ The exact sample size (*n*) for each experimental group/condition, given as a discrete number and unit of measurement
☐	☒ A statement on whether measurements were taken from distinct samples or whether the same sample was measured repeatedly
☐	☒ The statistical test(s) used AND whether they are one- or two-sided *Only common tests should be described solely by name; describe more complex techniques in the Methods section.*
☐	☒ A description of all covariates tested
☐	☒ A description of any assumptions or corrections, such as tests of normality and adjustment for multiple comparisons
☐	☒ A full description of the statistical parameters including central tendency (e.g. means) or other basic estimates (e.g. regression coefficient) AND variation (e.g. standard deviation) or associated estimates of uncertainty (e.g. confidence intervals)
☐	☒ For null hypothesis testing, the test statistic (e.g. *F*, *t*, *r*) with confidence intervals, effect sizes, degrees of freedom and *P* value noted *Give P values as exact values whenever suitable.*
☐	☒ For Bayesian analysis, information on the choice of priors and Markov chain Monte Carlo settings
☐	☒ For hierarchical and complex designs, identification of the appropriate level for tests and full reporting of outcomes
☐	☒ Estimates of effect sizes (e.g. Cohen's *d*, Pearson's *r*), indicating how they were calculated

Our web collection on statistics for biologists contains articles on many of the points above.

Software and code

Policy information about availability of computer code

Data collection	Data was collected with an Illumina sequencer and software (v Imaging data were acquired on a Metafer VSlide system and processed using VSlide software (v1.0.0)
Data analysis	Data analysis was performed with a combination of published packages and custom script, all of which can be found at https://github.com/marzamKI/spatial_atac The softwares used in this analysis are: CellRanger ATAC (v2.0.0) Loupe Browser (v6.0.0) SpaceRanger (v1.3.1) MACS2 (v2.2.6) DCA (v0.3.4) R (v4.2.0) bedtools (v2.19.0) Fiji (v2.3.0) The R packages used are: Seurat (v4.1.0) ArchR (v1.0.1) Harmony (v0.1.0) GenomicRanges (v1.46.1) STutility R package (v0.1.0) Signac (v1.6.0) EnsDb.Mmusculus.v79 (v2.99.0)

EnsDb.Hsapiens.v86 (v2.99.0)
gprofiler2 R package (v.0.2.1)
monocle3 (v1.0.0)

For manuscripts utilizing custom algorithms or software that are central to the research but not yet described in published literature, software must be made available to editors and reviewers. We strongly encourage code deposition in a community repository (e.g. GitHub). See the Nature Research guidelines for submitting code & software for further information.

Data

Policy information about availability of data

All manuscripts must include a data availability statement. This statement should provide the following information, where applicable:

- Accession codes, unique identifiers, or web links for publicly available datasets
- A list of figures that have associated raw data
- A description of any restrictions on data availability

Raw data and processed count matrices generated from the mouse samples can be found using the accession code GSE214991.
Human sequencing data are stored in the SciLife Data Repository and can be accessed at 10.17044/scilifelab.21378279.
Additionally, we analyzed published datasets, which can be found in Table S2.

Reference genomes used to map mouse and human data were obtained by 10X Genomics as part of their standard Cellranger ATAC pipeline (v2.0.0).

Field-specific reporting

Please select the one below that is the best fit for your research. If you are not sure, read the appropriate sections before making your selection.

☒ Life sciences ☐ Behavioural & social sciences ☐ Ecological, evolutionary & environmental sciences

For a reference copy of the document with all sections, see nature.com/documents/nr-reporting-summary-flat.pdf

Life sciences study design

All studies must disclose on these points even when the disclosure is negative.

Sample size	No sample size calculations were performed. The sample size used in this study is in the same range as other studies using similar technologies. For embryo spatial ATAC data, data for each developmental age was acquired in 2 replicates (i.e. adjacent tissue sections from the same specimen). For the human spatial ATAC data, we processed 3 replicates. Spatial transcriptomics was performed on 1 or 2 sections from the same tissue.
Data exclusions	Spatial ATAC and transcriptomics data were inspected on Loupe browser and filtered through manual selection of capture areas that were not underlying the tissue slice. Gene activity matrices computed from spatial chromatin data were filtered to exclude the large genes clusters Pcdh and Ugt.
Replication	We performed different types of data processing, including producing feature-barcode matrices using an ENCODE consensus peak set or following MACS2 peak calling, as well as denoising with DCA. Data processed in different ways were then used to assess clustering concordance across tissues and replicates, which always showed good overlap.
Randomization	There was no randomization applied in this study. Embryos from different pregnant mice were used to acquire spatial transcriptomics and ATAC data.
Blinding	Clustering of data was performed using unsupervised approaches.

Reporting for specific materials, systems and methods

We require information from authors about some types of materials, experimental systems and methods used in many studies. Here, indicate whether each material, system or method listed is relevant to your study. If you are not sure if a list item applies to your research, read the appropriate section before selecting a response.

Materials & experimental systems

n/a	Involved in the study
☐	☒ Antibodies
☒	☐ Eukaryotic cell lines
☒	☐ Palaeontology and archaeology
☐	☒ Animals and other organisms
☐	☒ Human research participants
☒	☐ Clinical data
☒	☐ Dual use research of concern

Methods

n/a	Involved in the study
☒	☐ ChIP-seq
☒	☐ Flow cytometry
☒	☐ MRI-based neuroimaging

Antibodies

Antibodies used	Primary antibodies: - rabbit anti-SOX2 Merck 5603 - goat anti-SOX9 R&D 3075 - anti-nuclear antigen Novus 235-1. Secondary antibodies: - Donkey anti-Rabbit IgG (H+L) Highly Cross-Adsorbed Secondary Antibody, Alexa Fluor™ 647, Thermo 31573 - Donkey anti-Goat IgG (H+L) Cross-Adsorbed Secondary Antibody, Alexa Fluor™ 647, Thermo 21447
Validation	Anti-SOX2: multiple citations of use in mouse tissues in the website from the manufacturer e.g. PMID 26315499 Anti-SOX9: multiple citations of use in mouse tissues in the website from the manufacturer e.g. PMID 35294885 Novus 235-1: multiple citations of use in mouse tissues in the website from the manufacturer e.g. PMID 34912114

Animals and other organisms

Policy information about studies involving animals; ARRIVE guidelines recommended for reporting animal research

Laboratory animals	Time pregnant mice were from the strain C57BL/6JRj and were obtained from Janvier. Embryos were collected at embryonic days 12.5, 13.5, and 15.5. Embryo sex was not determined. Mice were housed with a standard light/dark cycle and availability of food and water ad libitum.
Wild animals	The study did not involve wild animals
Field-collected samples	The study did not involve field-collected samples
Ethics oversight	All experimental procedures were carried out in accordance to the Swedish and European Union guidelines and approved by the institutional ethical committee in Stockholm County (Stockholms Norra Djurförsöksetiska Nämnd) under ethical permit numbers N155/16 and 20785/2020.

Note that full information on the approval of the study protocol must also be provided in the manuscript.

Human research participants

Policy information about studies involving human research participants

Population characteristics	Breast cancer tissue from one patient was obtained from the Department of Clinical Pathology and Cancer Diagnostics at Karolinska University Hospital, Stockholm, Sweden. Age at diagnosis: 88. Tumor subtype: HER2-positive non-luminal. NHG grade: 3. Tumor size: 30mm. Histological subtype: invasive ductal carcinoma. Lymph node methastasis: yes. Provided in Table S3.
Recruitment	Informed consent was obtained from the participating patient.
Ethics oversight	Experimental procedures and protocols were approved by the regional ethics review board (Etikprövningsnämnden) in Stockholm (2016/957-31, amendment 2017/742-32 and 2021-00795), and informed consent was obtained from the participating patient.

Note that full information on the approval of the study protocol must also be provided in the manuscript.